Nanoscale Horizons

ROYAL SOCIETY OF CHEMISTRY

COMMUNICATION

View Article Online
View Journal | View Issue

Cite this: *Nanoscale Horiz.*, 2025, **10**, 586

Received 2nd September 2024,
Accepted 2nd January 2025

DOI: 10.1039/d4nh00437j

rsc.li/nanoscale-horizons

Spillover of active oxygen intermediates of binary RuO_2/Nb_2O_5 nanowires for highly active and robust acidic oxygen evolution†

Linqing Liao,‡[ab] Wangyan Gou,‡[c] Mingkai Zhang,[d] Xiaohe Tan,[ab] Zening Qi,[e] Min Xie,[e] Yuanyuan Ma*[ab] and Yongquan Qu *[ab]

Over-oxidation of surface ruthenium active sites of RuO_x-based electrocatalysts leads to the formation of soluble high-valent Ru species and subsequent structural collapse of electrocatalysts, which results in their low stability for the acidic oxygen evolution reaction (OER). Herein, a binary RuO_2/Nb_2O_5 electrocatalyst with abundant and intimate interfaces has been rationally designed and synthesized to enhance its OER activity in acidic electrolyte, delivering a low overpotential of 179 mV at 10 mA cm^{-2}, a small Tafel slope of 73 mV dec^{-1}, and a stabilized catalytic durability over a period of 750 h. Extensive experiments have demonstrated that the spillover of active oxygen intermediates from RuO_2 to Nb_2O_5 and the subsequent participation of lattice oxygen of Nb_2O_5 instead of RuO_2 for the acidic OER suppressed the over-oxidation of surface ruthenium species and thereby improved the catalytic stability of the binary electrocatalysts.

New concepts

The lattice oxygen mechanism (LOM) can break the scale relationship of Ru-based electrocatalysts for the acidic oxygen evolution reaction (OER) through the involvement of lattice oxygen, which can greatly enhance the activity. However, the generation of surface high-valent ruthenium species accompanied by the formation of oxygen vacancies leads to dissolution of surface Ru species and then decay of catalytic activity. Herein, we designed and synthesized a binary RuO_2/Nb_2O_5 nanowire catalyst with intimate interfaces, which enabled the spillover of the reactive intermediate *O from RuO_2 to Nb_2O_5 and thereby delivered significantly improved activity and durability for the acidic OER. Combination of various *in situ* and *ex situ* techniques demonstrated the occurrence of the spillover of active oxygen intermediates from RuO_2 to Nb_2O_5 and the subsequent participation of lattice oxygen of Nb_2O_5 instead of RuO_2 for the acidic OER, thereby suppressing the over-oxidation of surface ruthenium species. We anticipate that this work can be beneficial in stimulating the study of oxygen spillover at the interface of binary oxide catalysts for designing high performance OER electrocatalysts.

Introduction

The rational design and synthesis of Ru-based acidic OER electrocatalysts with low overpotential and high durability are essential for the development of electrocatalytic hydrogen generation from water electrolysis in acidic media.[1,2] Previous investigations have suggested that the surface Ru species of RuO_2 tend to be over-oxidized during the acidic OER and generate the soluble high valent Ru species under external potentials of over 1.4 V.[1,3,4] Especially, defective RuO_x has been reported to deliver high catalytic activity for the acidic OER, which has been recognized to undergo a lattice oxygen mediated (LOM) pathway.[3,5–7] Participation of lattice oxygen leads to the formation of oxygen vacancies and subsequent production of high valent Ru species, thereby unavoidably inducing the serious dissolution of surface electroactive high-valent Ru species and consequent collapse of the crystal structure of the highly defective RuO_x-based electrocatalysts during the long-term operation. Thus, it's highly expected that new strategies to realize high performance Ru-based electrocatalysts for acidic OER can be developed.

To address this challenge, various interfacial and structural engineering strategies have been developed to modulate the valence state of Ru and suppress the over-oxidation of surface Ru species, including the hybridization of Ru-based catalysts with other components, chemical doping, formation of solid solution, *etc.*[8–11] Moreover, alternating between the LOM pathway of the defective RuO_x-based electrocatalysts and adsorbate

[a] *Research & Development Institute of Northwestern Polytechnical University in Shenzhen, Shenzhen, 518057, China. E-mail: yyma@nwpu.edu.cn, yongquan@nwpu.edu.cn*
[b] *Key Laboratory of Special Functional and Smart Polymer Materials of Ministry of Industry and Information Technology, School of Chemistry and Chemical Engineering, Northwestern Polytechnical University, Xi'an, 710072, China*
[c] *School of Materials Engineering, Xi'an Aeronautical University, Xi'an, 710077, China*
[d] *School of Science, Xi'an University of Technology, Xi'an, 710048, China*
[e] *Xi'an Yiwei Putai Environmental Protection Co., Ltd, Xi'an, 710065, China*

† Electronic supplementary information (ESI) available. See DOI: https://doi.org/10.1039/d4nh00437j

‡ These authors contributed equally to this study.

evolution mechanism (AEM) pathway or oxide path mechanism (OPM) also showed the potential to enhance the catalytic activity and durability of Ru-based catalysts for the acidic OER.[3,8,12,13] However, the catalytic performances were still far below the expectations for the practical applications, and part of the above-mentioned methodologies improved the catalytic stability of Ru-based electrocatalysts at the expense of activity.[14–16] Recently, the spillover of active oxygen intermediates has been proposed as a promising strategy to simultaneously enhance the activity and stability of IrO_x-based OER electrocatalysts in acidic electrolyte.[17] We recently reported the spillover of active oxygen intermediates from RuO_2 to MoO_3 in the binary RuO_2/MoO_3 electrocatalysts for the enhanced OER activity and stability in acidic electrolyte.[18] In this approach, MoO_3 with a low solubility in acidic media was integrated with RuO_2, in which the active oxygen species was initially generated on the surface active sites of RuO_2 and then spilled over towards MoO_3 for the release of oxygen. The spillover of the active oxygen species from RuO_2 to MoO_3 for the subsequent release of oxygen can avoid the generation of oxygen vacancies on RuO_2 and consequently suppresses the over-oxidation of surface Ru species, which theoretically improves the catalytic activity and stability. To date, only a few electrocatalysts have been reported to realize the simultaneously improved activity and stability for the acidic OER through the oxygen spillover strategy. To investigate the universal applicability of the oxygen spillover strategy for enhancing the acidic OER performance of RuO_2, the exploration of new binary electrocatalysts is anticipated.

Herein, a binary electrocatalyst of ruthenium oxide and niobium oxide nanowire (RuO_2/Nb_2O_5) was synthesized *via* a facile electrospinning/thermal treatment approach. RuO_2/Nb_2O_5 delivered a remarkable low overpotential of 176 mV at a current density of 10 mA cm^{-2}, a Tafel slope of 73 mV dec^{-1}, and a mass activity of 296 A g^{-1}, suggesting substantially superior catalytic performance in comparison to commercial RuO_2. Furthermore, RuO_2/Nb_2O_5 demonstrated an exceptional stability, enduring for at least 750 h in 0.5 M H_2SO_4. The *S*-numbers of RuO_2/Nb_2O_5 (3.01×10^5) and C-RuO_2 (1.07×10^3) indicated a significantly reduced dissolution rate of ruthenium in RuO_2/Nb_2O_5. Extensive experiments demonstrated that the integration of Nb_2O_5 and RuO_2 effectively inhibited the over-oxidation of surface Ru species and avoided the dissolution of Ru of the binary electrocatalysts for the acidic OER. Catalytic mechanism studies suggested the occurrence of spillover of the active oxygen species from RuO_2 to Nb_2O_5 during the acidic OER. Such a binary electrocatalyst broke the dilemma between the activity and stability of Ru-based electrocatalysts by preserving lower oxidation states of surface Ru species for a long period in the acidic OER.

Synthesis and characterization of RuO_2/Nb_2O_5

The synthetic process of the RuO_2/Nb_2O_5 binary nanowire electrocatalysis involves electron-spinning and subsequent thermal treatment at various temperatures. The details can be found in the ESI.† Typically, the nanowire-like precursors were prepared by electro-spinning of a polyvinyl pyrrolidone (PVP) solution containing $RuCl_3$ and $NbCl_5$ in the desired molar ratios. Then, calcination under a flow of air removed the polymers and transformed the wire-like precursors into binary oxide catalysts.[19]

Three RuO_2/Nb_2O_5 electrocatalysts were synthesized with the Ru/(Ru + Nb) molar ratios of 0.7, 0.6, and 0.5, which were determined using inductively coupled plasma emission spectrometry (ICP-ES, Table S1, ESI†). The catalysts were named RuO_2/Nb_2O_5-*x*, where *x* represented the molar ratio of Ru/(Ru + Nb). The transmission electron microscopy (TEM) image demonstrated the nanowire-like morphology of the binary RuO_2/Nb_2O_5-0.6 electrocatalysts (treated at 400 °C) with an average diameter of ~100 nm (Fig. 1a). The electrocatalysts were composed of small nanoparticles, indicating the highly accessible surface and largely exposed active sites for electrocatalysis. High-resolution TEM (HRTEM) images of RuO_2/Nb_2O_5-0.6 revealed a crystal structure with a lattice fringe spacing of 0.32 nm, which corresponded to the (110) lattice plane of rutile phase RuO_2 (Fig. 1b),[20] while no lattice fringe information of Nb_2O_5 was found, which could be attributed to the poor crystalline structure and small size of Nb_2O_5 in the catalysts. Fig. 1c showed the X-ray diffraction (XRD) patterns of RuO_2/Nb_2O_5-0.6 and RuO_2. RuO_2 was synthesized through the identical approach of RuO_2/Nb_2O_5 in the absence of the Nb precursor (Fig. S1, ESI†). The characteristic peaks of RuO_2 and RuO_2/Nb_2O_5 electrocatalysts matched well with the database profile of RuO_2 (rutile phase, PDF#: 97-064-7373), suggesting the formation of rutile phase RuO_2 in the catalysts.[21] The absence of characteristic XRD peaks of Nb_2O_5 further indicated the poorly crystallized and/or small Nb_2O_5 particles in the electrocatalysts. Energy-dispersive X-ray spectroscopy (EDS) elemental mapping images suggested the uniform distribution of Ru, Nb and O in a single nanowire of RuO_2/Nb_2O_5-0.6, demonstrating the presence of Nb in the electrocatalyst (Fig. 1d). As shown in Table S2 (ESI†), the atomic and weight ratios of Ru/(Ru + Nb) in RuO_2/Nb_2O_5-0.6 derived from EDS elemental mapping images were 0.63 and 0.65, respectively, which were close to the results of ICP (0.59 and 0.62). Similar EDS and ICP results further indicated that the distribution of elements within the catalyst was uniform. To further determine the formation of a binary structure of the electrocatalyst, Raman spectra of RuO_2, Nb_2O_5 and RuO_2/Nb_2O_5-0.6 were recorded and analyzed. In the Raman spectrum of RuO_2/Nb_2O_5-0.6, the characteristic peaks at 517 and 624 cm^{-1} corresponded to the E_g and A_{1g} vibrational modes of RuO_2, respectively (Fig. 1e).[22] The broad peak surrounding at 748 cm^{-1} was attributed to the Nb–O vibrational peak of Nb_2O_5. In comparison with the characteristic peak of highly crystalline commercial Nb_2O_5 appearing at 693 cm^{-1}, the blue-shift and broadening of the characteristic peak of the RuO_2/Nb_2O_5-0.6 catalysts by nearly 50 cm^{-1} suggested the poor crystalline and small size of Nb_2O_5 in the binary electrocatalysts.[23]

Catalytic performance

Initially, the catalytic performance of a series of RuO_2/Nb_2O_5 electrocatalysts was evaluated in a three-electrode electrolytic

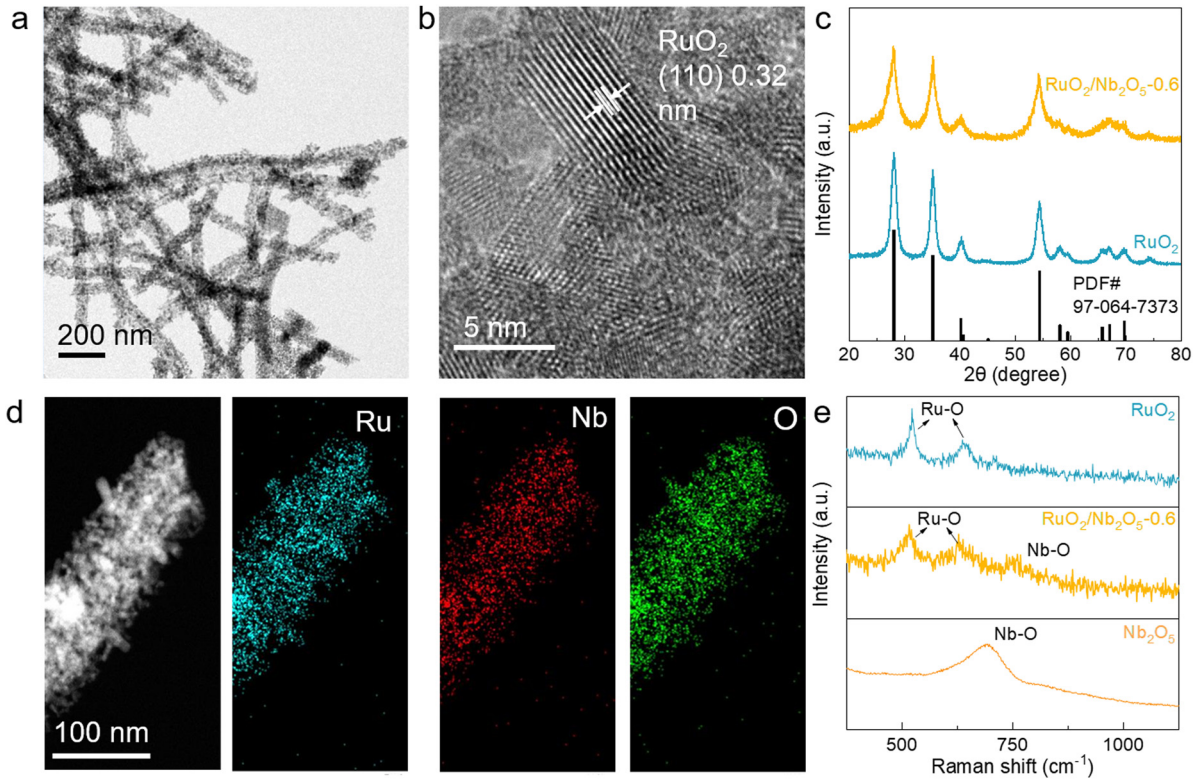

Fig. 1 Characterization studies of RuO_2/Nb_2O_5-0.6. (a) TEM image of RuO_2/Nb_2O_5-0.6. (b) HRTEM image of RuO_2/Nb_2O_5-0.6. (c) XRD patterns of RuO_2/Nb_2O_5-0.6 and RuO_2. (d) Elemental X-ray mappings of RuO_2/Nb_2O_5-0.6. (e) Raman spectra of RuO_2/Nb_2O_5-0.6, RuO_2 and Nb_2O_5.

cell with 0.5 M H_2SO_4 as the electrolyte, in which graphite rod and $Hg/Hg_2Cl_2/KCl$ electrode were employed as the counter and reference electrodes, respectively. All electrode potentials were calibrated and normalized to the reversible hydrogen electrode (RHE). After calcination under different temperatures, various RuO_2/Nb_2O_5 electrocatalysts were synthesized, exhibiting similar morphological features and the same crystal phase (Fig. 1 and Fig. S2–S5, ESI†). Afterwards, the catalytic performance of the prepared catalysts was analyzed to screen out the optimal composition and treatment temperature. As shown in Fig. S6 and S7 (ESI†), the RuO_2/Nb_2O_5-0.6 electrocatalyst treated at 400 °C delivered the best OER activity with the lowest overpotential of 179 mV at 10 mA cm^{-2} and the smallest Tafel slope of 73 mV dec^{-1}, which was identified as the optimal electrocatalyst in this work. Then, RuO_2, the commercially available Nb_2O_5 and RuO_2 (C-RuO_2) catalysts, as well as the electron-spun RuO_2 electrocatalysts synthesized through the identical process of RuO_2/Nb_2O_5-0.6 were selected as the control catalysts to highlight the importance and roles of Nb_2O_5 in improving catalytic performance of RuO_2/Nb_2O_5-0.6. As shown in their linear voltammetry scanning (LSV) curves (Fig. 2a), the bare OER activity of Nb_2O_5 was observed, indicating the catalytic inertness of Nb_2O_5. Comparatively, the RuO_2/Nb_2O_5-0.6 catalysts delivered the lowest overpotential of 179 mV at a current density of 10 mA cm^{-2}, which was much lower than those of RuO_2 (215 mV) and C-RuO_2 (256 mV). The catalytic current density of RuO_2/Nb_2O_5-0.6 at 1.5 V was 75.2 mA cm^{-2}, which was 2.7 times higher than that of the electron-spun RuO_2 electrocatalysts (27.9 mA cm^{-2}) and 6.1 times higher than that of the commercial C-RuO_2 electrocatalysts (12.3 mA cm^{-2}). The reaction kinetics were further evaluated by the derived Tafel slopes. The Tafel slope of RuO_2/Nb_2O_5-0.6 (73 mV dec^{-1}) was significantly lower than that of RuO_2 (107 mV dec^{-1}) and C-RuO_2 (164 mV dec^{-1}), indicating that the combination of ruthenium oxide and niobium oxide significantly enhanced the OER kinetics of the binary electrocatalysts (Fig. 2b).

In order to explore the intrinsic activity of the catalysts, the electrochemically active surface area (ECSA) was calculated from the electrochemical double layer capacitance (C_{DL}) by cyclic voltammetry (CV) tests (Fig. S8, ESI†).[24] After analyzing and fitting the data, the C_{DL} values of various electrocatalysts were calculated to be 2.73, 5.18 and 11.89 mF for the commercial C-RuO_2, RuO_2 and RuO_2/Nb_2O_5-0.6, respectively. C_S was the capacitance of an atomically smooth planar surface, which was 0.06 mF cm^{-2} in acidic media.[25] According to ECSA = C_{DL}/C_S, the RuO_2/Nb_2O_5-0.6 electrocatalysts possessed the highest ECSA of 198.2 cm^2, which was significantly higher than that of RuO_2 (86.4 cm^2) and commercial RuO_2 (45.5 cm^2).[24] By normalizing with the respective ECSA, the RuO_2/Nb_2O_5-0.6 electrocatalysts delivered the highest intrinsic OER activity of 200 mV at 0.1 mA cm_{ECSA}^{-2} under the acidic electrolyte, in comparison with that of RuO_2 (210 mV at 0.1 mA cm_{ECSA}^{-2}) and commercial C-RuO_2 (217 mV at 0.1 mA cm_{ECSA}^{-2}).

In addition, the turnover frequency (TOF) served as a pivotal metric for assessing catalyst activity. At an applied potential of 1.5 V, the TOF value of RuO_2/Nb_2O_5-0.6 reached 7.7 s^{-1},

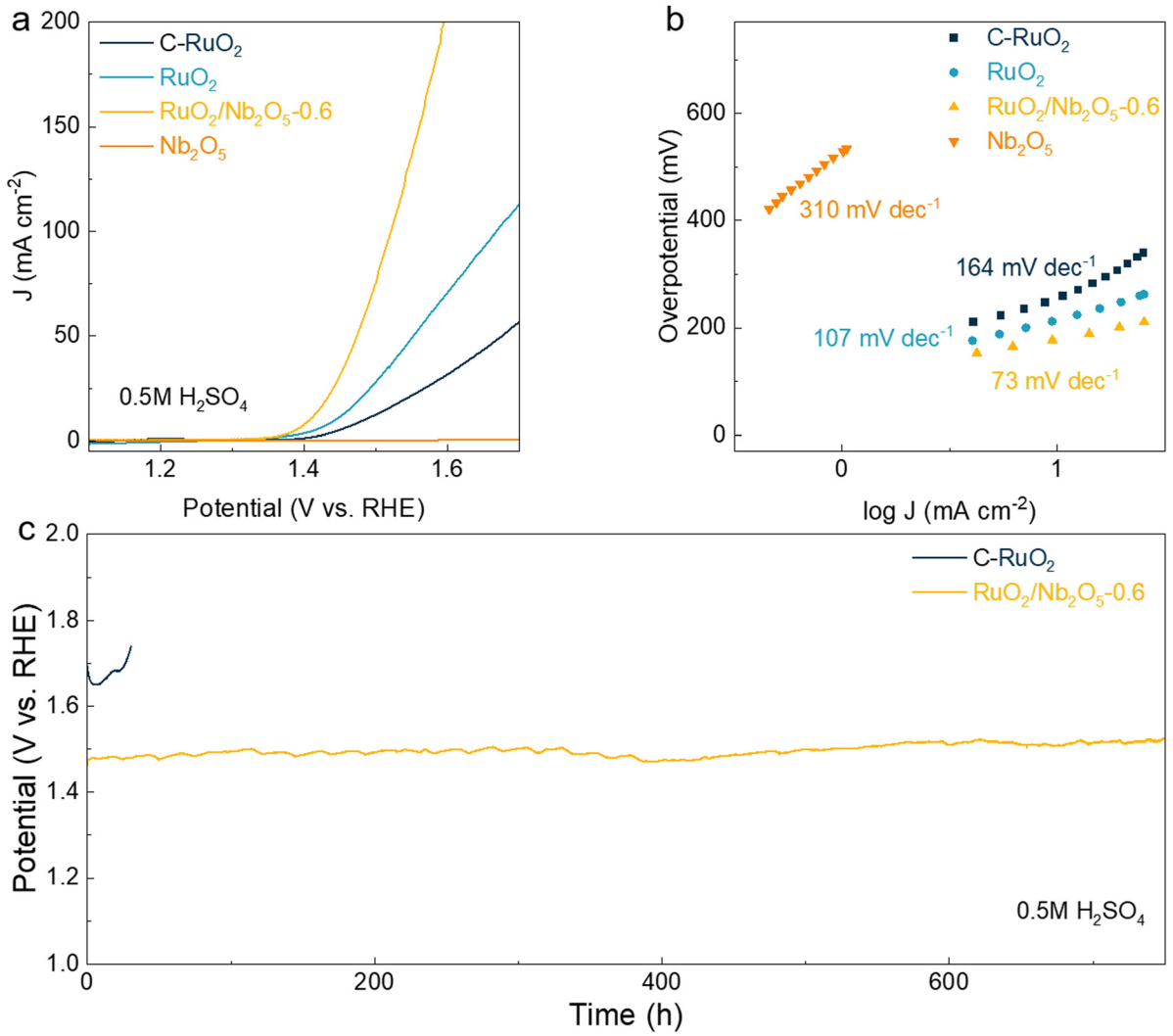

Fig. 2 Catalytic performance of various electrocatalysts in 0.5 M H_2SO_4 electrolyte. (a) LSV curves of RuO_2/Nb_2O_5-0.6, RuO_2, C-RuO_2, and Nb_2O_5. (b) Tafel slopes of RuO_2/Nb_2O_5-0.6, RuO_2, C-RuO_2, and Nb_2O_5. (c) Chronopotentiometry tests of RuO_2/Nb_2O_5-0.6 and C-RuO_2.

representing an almost sevenfold increase compared to RuO_2 (1.7 s^{-1}) and tenfold enhancement in comparison to C-RuO_2 (0.7 s^{-1}), as illustrated in Fig. S9a (ESI†). Moreover, the mass activity of RuO_2/Nb_2O_5-0.6 was 296 A g^{-1} at 1.5 V, surpassing that of RuO_2 (73 A g^{-1}) and C-RuO_2 (30 A g^{-1}), as depicted in Fig. S9b (ESI†). These significantly elevated TOF values and mass activities illustrated the enhanced intrinsic activity of RuO_2/Nb_2O_5-0.6 through the incorporation of Nb_2O_5.

The d-band of various catalysts, which was directly related to the strength of interaction between the Ru and guest molecules, was also determined by high-resolution valence-band (VB) XPS spectra. As shown in Fig. S10 (ESI†), our findings revealed that the d-band center of RuO_2/Nb_2O_5-0.6 was located at −1.53 eV, positioning it midway between C-RuO_2 (−1.55 eV) and RuO_2 (−1.48 eV). It was noteworthy that the closer proximity of the d-band center to the Fermi level implied a stronger binding strength between the catalyst and the adsorbed intermediates, which could be inconducive to their desorption.[26] Therefore, RuO_2/Nb_2O_5-0.6 showed a balanced adsorption capacity for these intermediates, ultimately contributing to its high activity.

Stability was another key parameter of electrocatalysts. The chronopotentiometry (CP) test was employed to assess the OER stability of RuO_2/Nb_2O_5-0.6, which exhibited high catalytic durability during a period of 750 h at a constant current density of 10 mA cm^{-2} (Fig. 2c). The performance of RuO_2/Nb_2O_5-0.6 was superior to that of the majority of recently reported Ru-based electrocatalysts in acidic electrolytes (Table S3, ESI†). Negligible decay was observed for RuO_2/Nb_2O_5-0.6. Based on the results of the ICP-ES tests, the *S*-numbers ($S = n_{O_2}/n_{Ru}$) of various catalysts at 10 mA cm^{-2} were calculated according to a previous report.[27] Compared to that of C-RuO_2 (1.07×10^3), the *S*-number of RuO_2/Nb_2O_5-0.6 was as high as 3.01×10^5, indicating that the dissolution of Ru was significantly suppressed during the long-term operation. Characterization studies on the spent catalysts indicated the preserved structural features of RuO_2/Nb_2O_5-0.6 during the OER (Fig. S11–S13, ESI†).

These results demonstrated the high chemical and structural stability and suppressed Ru dissolution of RuO_2/Nb_2O_5-0.6 for the acidic OER.

Chemical state analysis

To understand the influence of Nb on the electronic structures of RuO_2/Nb_2O_5-0.6 and their roles in the catalytic activity, chemical states of Ru were analyzed by using X-ray photoelectron spectroscopy (XPS, Fig. 3). For RuO_2/Nb_2O_5-0.6, the peak with a binding energy of 462.6 eV could be categorized as the 3p XPS characteristic peak of Ru^{4+}, which was shifted to the lower binding energy by 0.2 eV compared with those of RuO_2 and C-RuO_2 (at 462.8 eV).[28,29] Niobium 3d XPS spectroscopy showed that the RuO_2/Nb_2O_5-0.6 shifted to the lower binding energy by 0.5 eV (from 207.1 to 206.6 eV) compared to Nb_2O_5. The fitted deconvolution spectra of Nb contained $3d_{5/2}$ and $3d_{3/2}$ peaks in Nb_2O_5, which represented the Nb^{5+} states at 207.1 and 209.9 eV, respectively.[30] The Nb^{4+} peaks were also observed for RuO_2/Nb_2O_5-0.6 with a derived Nb^{4+}/Nb^{5+} ratio of 0.92 for RuO_2/Nb_2O_5-0.6, indicating the presence of abundant oxygen vacancy in the as-synthesized RuO_2/Nb_2O_5-0.6 electrocatalysts. In addition, the O 1s XPS spectra of various electrocatalysts were deconvoluted into lattice oxygen (O_L), oxygen atoms adjacent to defects (O_V) and hydroxyls (O_H).[31] The binding energy for lattice oxygen of the RuO_2/Nb_2O_5-0.6 was located at 530 eV, which was shifted towards higher binding energy by 0.5 eV compared to the synthetic RuO_2 and commercial C-RuO_2 (529.5 eV). The positive shift of the lattice oxygen indicated the transfer of electrons from lattice oxygen to metal sites, which reduced the oxidation state of Ru and Nb. The characteristic peaks located at 530.7 eV and 532.1 eV were attributed to O_V and O_H, respectively. The proportion of O_H of RuO_2/Nb_2O_5-0.6 (O_H/O_V = 1.49) was considerably higher than that of commercial C-RuO_2 (O_H/O_V = 0.94) and RuO_2 (O_H/O_V = 1.02).[32] Furthermore, the O_H/O_V value of RuO_2/Nb_2O_5-0.6 was higher than that of RuO_2/Nb_2O_5-0.5 (0.68) and RuO_2/Nb_2O_5-0.7 (1.08). This finding illustrated that the binary electrocatalysts exhibited higher catalytic activity, accompanied by a larger O_H/O_V ratio, among catalysts with varying amounts of Nb_2O_5 introduced (Fig. S14 and Table S4, ESI†). The enhanced hydroxyl adsorption with defects at the active sites modulated the adsorption energy of the oxygen intermediates and enhanced the catalytic activity and stability of RuO_2/Nb_2O_5-0.6.

Catalytic mechanism

To investigate the reaction mechanism of the binary RuO_2/Nb_2O_5 electrocatalysts, the pH-dependent tests of various catalysts were performed and compared (Fig. 4a). In contrast to the coupled proton–electron transfer step in the AEM pathway of bare RuO_2 with good crystallinity, the LOM pathway breaks this scaling relationship, where the proton transfer step becomes the potential-determining step (PDS).[33] Therefore, the pH-dependent kinetics of RuO_2/Nb_2O_5-0.6 sufficiently reflected the participation of lattice oxygen in the OER procedure, indicating the LOM pathway for the OER. When the relationship was further compared at 1.5 V, a linear relationship was fitted by a linear fit between the logarithm of the current density and the pH values. The proton reaction orders derived from the slope ($\rho = (\partial(\log i)/\partial \mathrm{pH})_E$) were 0.8 and 0.4 for RuO_2/Nb_2O_5 and C-RuO_2, respectively, confirming the dominant LOM pathway of RuO_2/Nb_2O_5-0.6 for the acidic OER.[34] In order to probe the PDS of the binary electrocatalysts, isotope experiments with 0.5 M H_2SO_4 in the H_2O and D_2O as solvents were performed. The Tafel slope of RuO_2/Nb_2O_5 significantly increased from 84 mV dec^{-1} in H_2O to 142 mV dec^{-1} in D_2O, suggesting that the deprotonation process was PDS of the binary catalysts,[35] while the Tafel slopes of the commercial RuO_2 showed a minor change for the isotope experiments, indicating that the AEM pathway was dominant (Fig. 4b).

To further reveal the OER reaction mechanism of the binary catalysts, *operando* Fourier transform infrared (FTIR) spectroscopy was employed to monitor the reaction intermediates. When the applied potential exceeded the reaction onset potential of the C-RuO_2 electrocatalysts (>1.3 V), a pair of the distinguishable absorption peaks located at 1050 cm^{-1} and 1150 cm^{-1} were observed (Fig. 4c). The pair absorption peaks were identified as

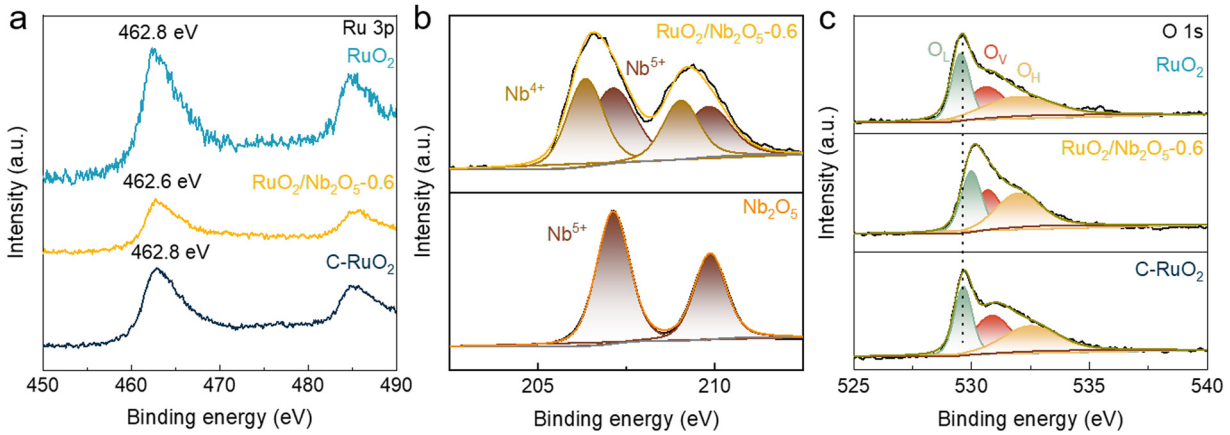

Fig. 3 XPS spectroscopies of catalysts. (a) Ru 3p XPS spectra of RuO_2/Nb_2O_5-0.6, RuO_2, C-RuO_2. (b) Nb 3d XPS spectra of RuO_2/Nb_2O_5-0.6, Nb_2O_5. (c) O 1s XPS spectra of RuO_2/Nb_2O_5-0.6, RuO_2, C-RuO_2.

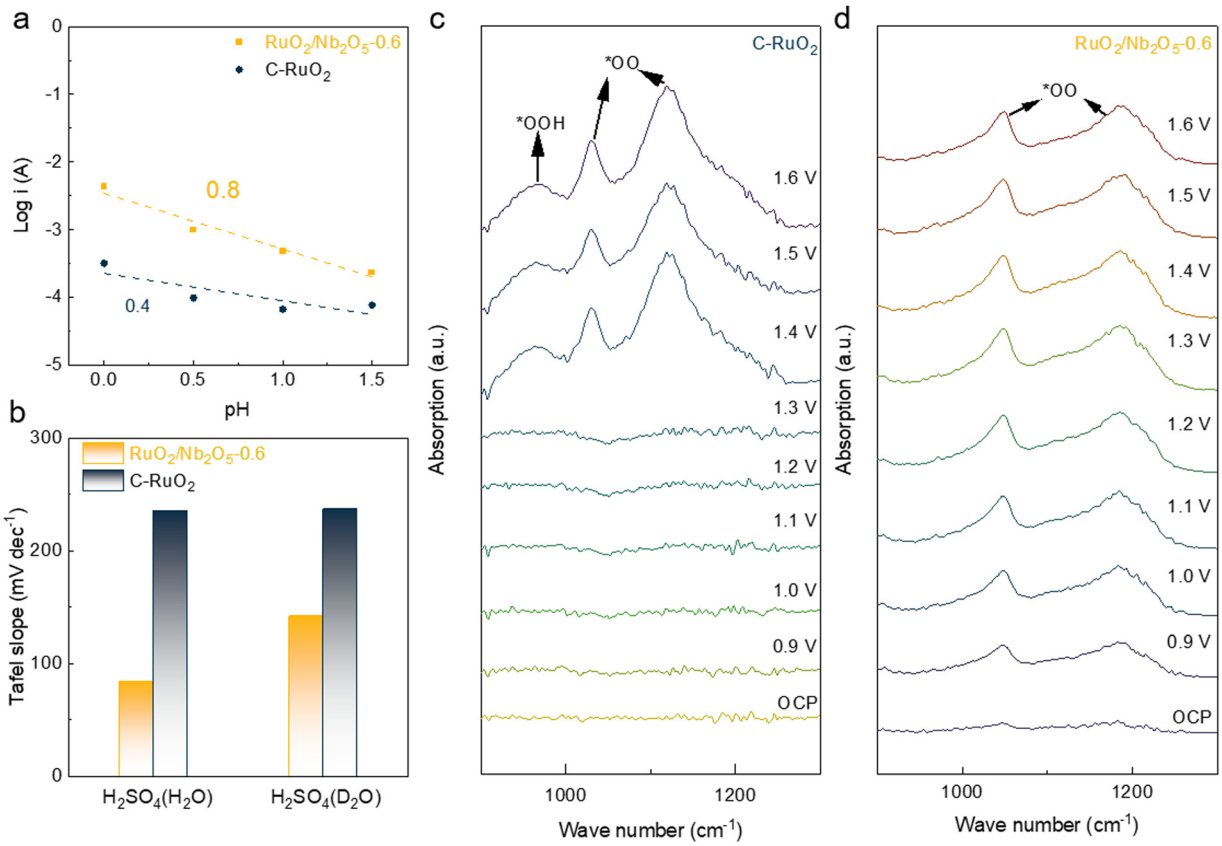

Fig. 4 Electrochemical mechanism tests of catalysts. (a) Current densities of RuO_2/Nb_2O_5-0.6 and C-RuO_2 at 1.5 V *versus* RHE as a function of the pH values of electrolytes. (b) Comparison of RuO_2/Nb_2O_5-0.6 and C-RuO_2 in 0.5 M H_2SO_4, where H_2O or D_2O was used as the solvent. (c) *Operando* FTIR spectra recorded in the potential range of 0.9–1.6 V *vs.* RHE for C-RuO_2. (d) *Operando* FTIR spectra recorded in the potential range of 0.9–1.6 V *vs.* RHE for RuO_2/Nb_2O_5-0.6.

OO*, which was an intermediate prior to the release of oxygen in the LOM approach. Generally, the absorption peak at 948 cm^{-1} was attributed to OOH* as a reaction intermediate in the AEM.[7] The dynamically enhanced peak intensity was observed, suggesting that the increase in the applied potential accelerated the generation of the reaction intermediates. The presence of the absorption peaks of OOH* and OO* in the C-RuO_2 catalysts was attributed to the coexistence of the LOM pathway and the AEM pathway in the acidic OER (Fig. 4c). However, only OO* adsorption peaks located at 1050 cm^{-1} and 1180 cm^{-1} were detected in the FTIR spectra of RuO_2/Nb_2O_5-0.6, suggesting that the catalytic pathway of the binary electrocatalysts was dominated by the LOM pathway for the acidic OER (Fig. 4d). The observation of OO* peaks at a lower potential of 0.9 V suggested high catalytic OER performance of the binary electrocatalysts with more reactive intermediates generated on the surface of RuO_2/Nb_2O_5-0.6. It has been widely recognized that surface Ru species of RuO_2 are converted to the higher oxidation state through the LOM pathway for the acidic OER, therefore leading to the formation of the soluble ruthenium species and subsequent decay of catalytic activity.

Next, the charge transfer that occurred between catalyst surfaces and electrolyte was investigated by electrochemical impedance spectroscopy (EIS) to understand the roles of Nb incorporated with RuO_2 for enhanced catalytic stability as well as activity. The Bode point plots of RuO_2/Nb_2O_5-0.6 and commercial C-RuO_2 with potentials from 1.1 V to 1.6 V are shown in Fig. S15 (ESI†), respectively. The characteristic peaks in the high frequency region (10^1–10^3 Hz) were attributed to the surface oxidation of the catalyst. The characteristic peaks in the low-frequency region (10^{-1}–10^1 Hz) reflected the adsorption of reaction intermediates on the surface of the catalyst.[36] For the C-RuO_2 catalysts, the phase angle decreased slowly in the low-frequency range with increasing potential, indicating that C-RuO_2 had insufficient capacity to adsorb intermediates[37,38] whereas the significantly decreased phase angle of RuO_2/Nb_2O_5-0.6 in the low frequency region suggested that the binary electrocatalysts showed less resistance to adsorb intermediates at the same voltage. The peak shape of C-RuO_2 significantly changed over 1.4 V, suggesting the unstable surface of C-RuO_2 with the increased potentials. In contrast, the barely changed characteristic peaks of RuO_2/Nb_2O_5-0.6 in the high-frequency region with the increased potentials revealed more stable surface oxidation states of Ru at higher potentials. The comparative results demonstrated high catalytic activity and stability of the binary RuO_2/Nb_2O_5-0.6 electrocatalysts for the acidic OER.

To further elucidate the enhanced catalyst stability, CV curves were recorded to examine the oxidation states of the surface Ru species during the acidic OER (Fig. 5a). Two sets of

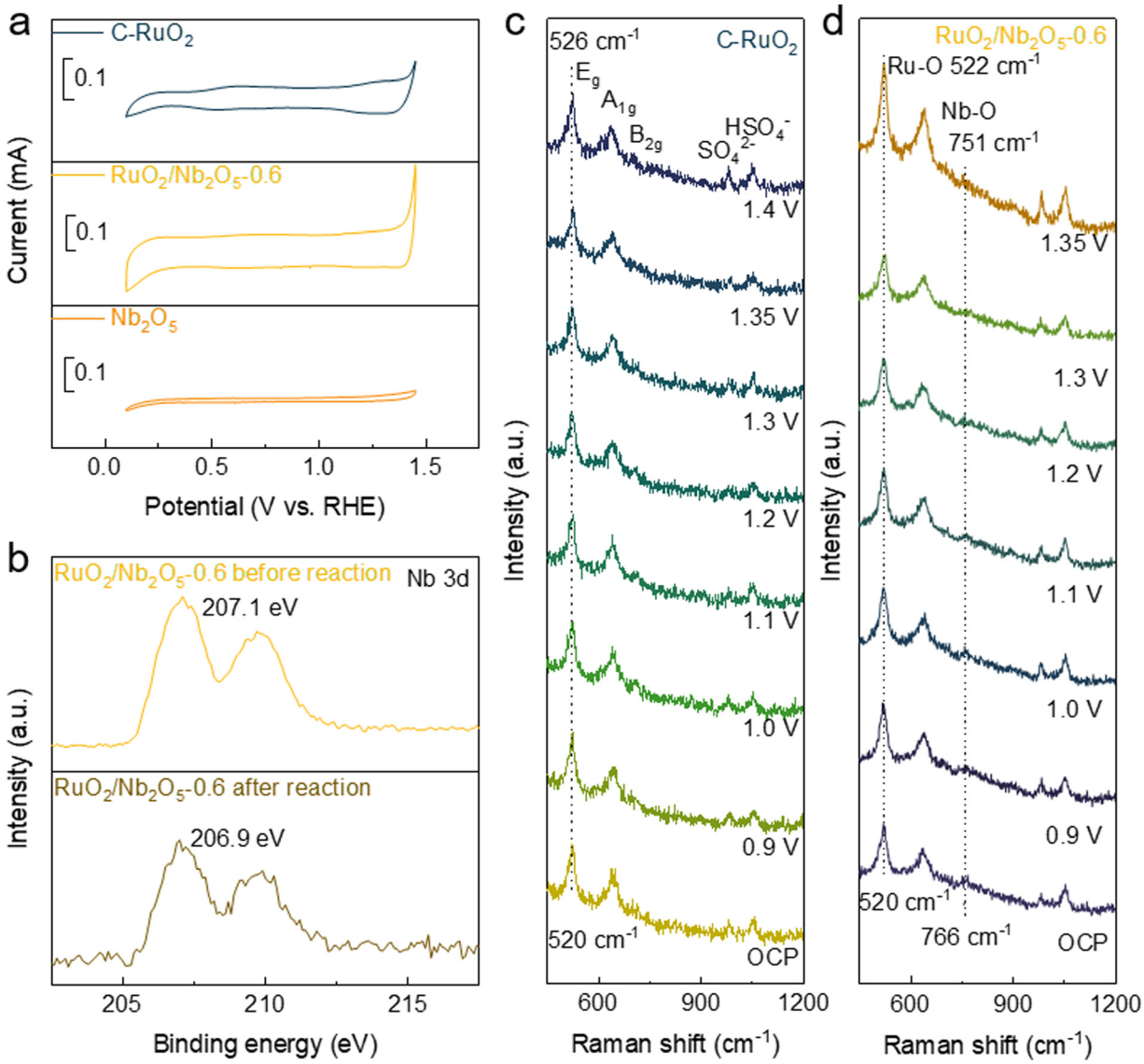

Fig. 5 Electrochemical stability analysis and evidence of oxygen spillover phenomena. (a) CV curves of RuO_2/Nb_2O_5-0.6, Nb_2O_5 and C-RuO_2 measured from 0.1 to 1.45 V *vs.* RHE. (b) Nb 3d XPS spectra of RuO_2/Nb_2O_5-0.6 before and after the stability test. *Operando* Raman spectra recorded in the potential range of 0.9–1.4 V *vs.* RHE for (c) C-RuO_2 and (d) RuO_2/Nb_2O_5-0.6.

redox peaks located around 0.6 V and 1.25 V were observed for the C-RuO_2 electrocatalysts, which represented $Ru^{3+/4+}$ and $Ru^{4+/6+}$ redox pairs, respectively.[39] Thus, the surface Ru species of C-RuO_2 could be oxidized into high valent Ru species, leading to the serious over-oxidation of catalysts and formation of soluble Ru species during the acidic OER.[40] Thus, it's not surprising to observe the poor catalytic stability of C-RuO_2. Comparatively, only the redox peaks of $Ru^{3+/4+}$ was observed for RuO_2/Nb_2O_5-0.6, indicating that the introduction of Nb effectively inhibited the over-oxidation of Ru in the catalyst and stabilized the binary electrocatalysts for the acidic OER. Afterwards, the chemical states of two catalysts before and after the acidic OER were analyzed by XPS. For the RuO_2/Nb_2O_5-0.6 catalyst, the binding energy of Ru 3p barely changed after 10 h of reaction at a current density of 10 mA cm^{-2}. In contrast, the Ru 3p binding energy of C-RuO_2 increased from 462.8 eV of the fresh electrocatalysts to 463 eV of the spent ones, indicating the over-oxidation of Ru species of C-RuO_2 (Fig. S16, ESI†). As shown in the XPS spectra of Nb 3d of RuO_2/Nb_2O_5-0.6 before and after the acidic OER, the peaks of Nb were negatively shifted by 0.2 eV, suggesting the formation of oxygen vacancies at the Nb site (Fig. 5b).[41] The electron transfer pathway in the LOM was based on a redox-catalyzed reaction of oxygen, in which lattice oxygen was electrochemically activated in the form of released oxygen intermediates, following the pathway OH^-–$(OO)^{2-}$–O_2, essentially a hybridization of neighbouring non-bonded oxygen atoms (O^-), with no transfer of electrons to the external circuit.[42] Thus, it's logical to predict the occurrence of spillover of O* intermediates from RuO_2 to Nb_2O_5 and the participation of lattice oxygen in Nb_2O_5 for the acidic OER, like in the previous reports.[18] In this way, the OO* intermediate was formed on Nb_2O_5 instead of RuO_2 for the steps of the release of

oxygen, generation of oxygen vacancies and rehabilitation of lattice oxygen. Therefore, the over-oxidation and dissolution of surface Ru species of the binary RuO_2/Nb_2O_5 electrocatalysts could be suppressed, which was consistent with the EIS profile (Fig. S15, ESI†) and CV results (Fig. 5a).

To investigate the potential of oxygen spillover in the binary electrocatalysts, oxygen temperature-programmed desorption (O_2-TPD) profiles were recorded for Nb_2O_5 and RuO_2 (Fig. S17, ESI†).[43] The desorption peak of oxygen from RuO_2 was observed at a significantly higher temperature of 431 °C compared to 303 °C for Nb_2O_5, suggesting that RuO_2 requires more energy for O_2 desorption than Nb_2O_5. The O_2-TPD results indicated that the formation of oxygen vacancies on Nb_2O_5 was more facile than RuO_2. Based on these findings, the thermodynamic feasibility of oxygen spillover involving the transfer of intermediate O* species from RuO_2 to Nb_2O_5 and the participation of lattice oxygen in Nb_2O_5 for the acidic OER, was established.

To experimentally confirm the occurrence of oxygen spillover, *in situ* Raman spectroscopy was used to dynamically monitor the surface M–O species of the RuO_2/Nb_2O_5-0.6 and C-RuO_2 catalysts at different external potentials. The characteristic peaks of Ru–O in C-RuO_2 were located at 520 cm^{-1}, 640 cm^{-1} and 705 cm^{-1}, which represented the E_g, A_{1g} and B_{2g} vibrational modes of Ru–O, respectively (Fig. 5c).[22,44] Since the characteristic peak of E_g was more obvious and the peak position was easier to be distinguished, the characteristic E_g peak of Ru–O of C-RuO_2 was mainly analyzed. As shown in Fig. 5c, the E_g peak of C-RuO_2 gradually shifted to the higher wavenumber by 6 cm^{-1} (from 520 cm^{-1} to 526 cm^{-1}) with the increased external applied voltage from the open-circuit potential to 1.6 V, indicating that the surface Ru–O bonds in C-RuO_2 were gradually compressed and the valence state of Ru was elevated progressively with the increased potentials.[45] As for RuO_2/Nb_2O_5-0.6, the characteristic peak of Ru–O was barely shifted with the increased potential, whereas the characteristic peak of Nb–O showed a redshift of 15 cm^{-1} (from 766 cm^{-1} to 751 cm^{-1}), indicating the significantly stretched Nb–O of the binary electrocatalysts (Fig. 5d).[17] The reduced oxidation state of Nb combined with the LSV and CV curves showed that Nb suppressed the elevation of the oxidation state of Ru during the oxygen evolution reaction through the modification of bonding with oxygen. Therefore, compared to C-RuO_2, the over-oxidation of Ru in RuO_2/Nb_2O_5-0.6 was noticeably suppressed, leading to the stabilized surface Ru species. Significantly, as the circuit was disconnected after applying 1.6 V for a period of time, the characteristic E_g peak of Ru–O in RuO_2/Nb_2O_5-0.6 gradually recovered to the initial state (522 cm^{-1}). Compared with the pristine binary electrocatalyst, the characteristic Raman peak of Nb–O also gradually restored to the same position before the reaction (763 cm^{-1}, Fig. S18, ESI†). These shifts further illustrated the structural stability of RuO_2/Nb_2O_5-0.6 in the acidic OER. Combined with the results of CV curves, XPS and *in situ* FT-IR, *in situ* Raman spectra strongly suggested the reactive oxygen species spilled over from RuO_2 to Nb_2O_5, consistent with the preserved E_g of Ru–O and shifted 15 cm^{-1} of Nb–O in the binary RuO_2/Nb_2O_5 electrocatalysts.

Based on all of the above analysis and experimental evidence, a catalytic pathway is proposed for RuO_2/Nb_2O_5-0.6 with high catalytic activity and stability through the LOM pathway (Fig. 6). Initially, water molecules are absorbed and activated on the surface Ru sites of the binary electrocatalysts to generate OH* species. After the deprotonation of OH*, the O* intermediates spill over from Ru sites to Nb sites. With the participation of the lattice oxygen of Nb_2O_5, OO* intermediates are formed on Nb sites, followed by the release of O_2 associated with the generation of oxygen vacancies and rehabilitation of lattice oxygen on Nb_2O_5. Such a catalytic pathway of RuO_2/Nb_2O_5 effectively suppresses the over-oxidation of Ru species and avoids the formation of soluble high valent Ru species, leading to the high catalytic activity and stability for the acidic OER despite undergoing the LOM mechanism.

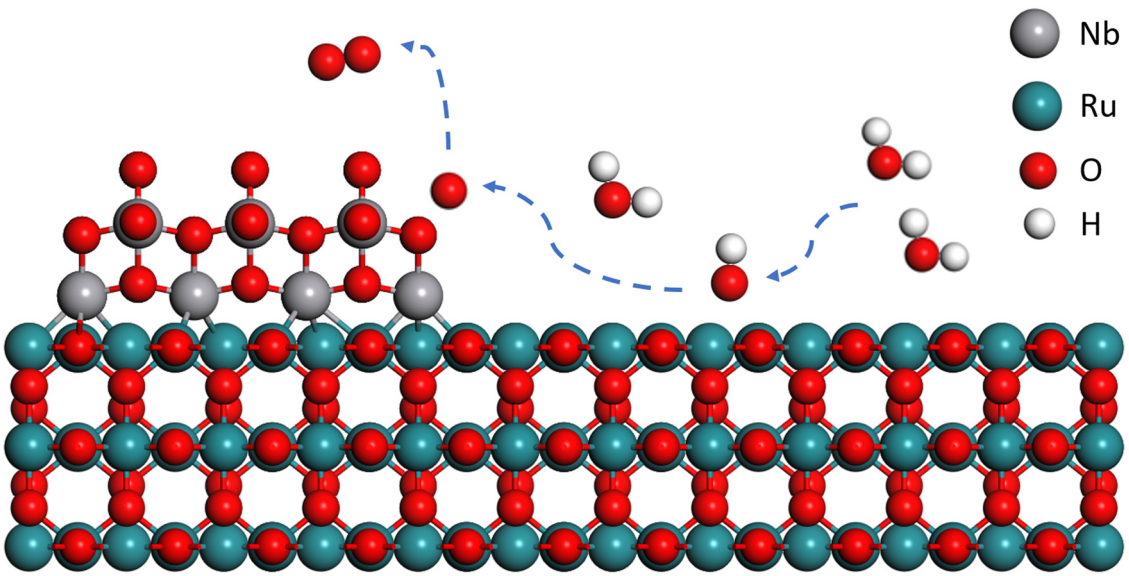

Fig. 6 Schematic overview of the proposed oxygen spillover for the OER on the surface of RuO_2/Nb_2O_5-0.6 catalysts.

Conclusions

In summary, we presented the highly active and robust binary RuO_2/Nb_2O_5 electrocatalysts for the acidic OER, delivering a low overpotential of 176 mV at 10 mA cm^{-2} and a high stability of at least 750 h in 0.5 M H_2SO_4. Incorporation of Nb_2O_5 with RuO_2 enabled the spillover of active O* intermediate from RuO_2 to Nb_2O_5. Thus, the participation of lattice oxygen of Nb_2O_5 instead of RuO_2 gave the OO* intermediate for the release of oxygen, which effectively inhibited the over-oxidation of surface Ru species and thereby significantly improved the catalytic stability of the binary electrocatalysts. Extensive experimental investigations verified the proposed oxygen spillover reaction pathway for the enhanced catalytic performance of the binary electrocatalysts. This work provided seminal insights into solving the stability problem of Ru-based catalysts and offered a methodology for the rational design of high performance electrocatalysts for the acidic OER.

Data availability

The data supporting this article have been included as part of the ESI.†

Conflicts of interest

The authors declare no competing financial interest.

Acknowledgements

The authors acknowledge the Basic and Applied Basic Research Foundation of Guangdong Province (2023A1515012288) and the Fundamental Research Funds for the Central Universities (D5000210829). Yongquan Qu acknowledges the Fundamental Research Funds for the Central Universities (D5000210601).

References

1 Q. Wang, Y. Cheng, H. B. Tao, Y. Liu, X. Ma, D. S. Li, H. B. Yang and B. Liu, *Angew. Chem., Int. Ed.*, 2023, **62**, e202216645.
2 L. Li, G. Zhang, C. Zhou, F. Lv, Y. Tan, Y. Han, H. Luo, D. Wang, Y. Liu, C. Shang, L. Zeng, Q. Huang, R. Zeng, N. Ye, M. Luo and S. Guo, *Nat. Commun.*, 2024, **15**, 4974.
3 X. Rong, J. Parolin and A. M. Kolpak, *ACS Catal.*, 2016, **6**, 1153–1158.
4 L. Li, P. Wang, Q. Shao and X. Huang, *Adv. Mater.*, 2021, **33**, 2004243.
5 C. Roy, R. R. Rao, K. A. Stoerzinger, J. Hwang, J. Rossmeisl, I. Chorkendorff, Y. Shao-Horn and I. E. L. Stephens, *ACS Energy Lett.*, 2018, **3**, 2045–2051.
6 N. Hodnik, P. Jovanovič, A. Pavlišič, B. Jozinović, M. Zorko, M. Bele, V. S. Šelih, M. Šala, S. Hočevar and M. Gaberščček, *J. Phys. Chem. C*, 2015, **119**, 10140–10147.
7 C. Lin, J.-L. Li, X. Li, S. Yang, W. Luo, Y. Zhang, S.-H. Kim, D.-H. Kim, S. S. Shinde, Y.-F. Li, Z.-P. Liu, Z. Jiang and J.-H. Lee, *Nat. Catal.*, 2021, **4**, 1012–1023.
8 R. Y. Fan, Y. S. Zhang, J. Y. Lv, G. Q. Han, Y. M. Chai and B. Dong, *Small*, 2024, **20**, e2304636.
9 L. Zhou, Y. Shao, F. Yin, J. Li, F. Kang and R. Lv, *Nat. Commun.*, 2023, **14**, 7644.
10 Z. Niu, Z. Lu, Z. Qiao, S. Wang, X. Cao, X. Chen, J. Yun, L. Zheng and D. Cao, *Adv. Mater.*, 2024, **36**, 2310690.
11 W. Gou, Y. Wang, M. Zhang, X. Tan, Y. Ma and Y. Qu, *Chin. J. Catal.*, 2024, **60**, 68–106.
12 Z. Feng, C. Dai, P. Shi, X. Lei, R. Guo, B. Wang, X. Liu and J. You, *Chem. Eng. J.*, 2024, **485**, 149992.
13 Z. Wang, W. A. Goddard and H. Xiao, *Nat. Commun.*, 2023, **14**, 4228.
14 Y. Wu, R. Yao, Q. Zhao, J. Li and G. Liu, *Chem. Eng. J.*, 2022, **439**, 135699.
15 Y. Xue, J. Fang, X. Wang, Z. Xu, Y. Zhang, Q. Lv, M. Liu, W. Zhu and Z. Zhuang, *Adv. Funct. Mater.*, 2021, **31**, 2101405.
16 J. Wang, C. Cheng, Q. Yuan, H. Yang, F. Meng, Q. Zhang, L. Gu, J. Cao, L. Li, S.-C. Haw, Q. Shao, L. Zhang, T. Cheng, F. Jiao and X. Huang, *Chem*, 2022, **8**, 1673–1687.
17 Z. Shi, J. Li, J. Jiang, Y. Wang, X. Wang, Y. Li, L. Yang, Y. Chu, J. Bai, J. Yang, J. Ni, Y. Wang, L. Zhang, Z. Jiang, C. Liu, J. Ge and W. Xing, *Angew. Chem., Int. Ed.*, 2022, **61**, e202212341.
18 W. Gou, S. Zhang, Y. Wang, X. Tan, L. Liao, Z. Qi, M. Xie, Y. Ma, Y. Su and Y. Qu, *Energy Environ. Sci.*, 2024, **17**, 6755–6765.
19 X. Tan, M. Zhang, D. Chen, W. Li, W. Gou, Y. Qu and Y. Ma, *Small*, 2023, **19**, e2303249.
20 J. Okal and M. Zawadzki, *Appl. Catal., B*, 2009, **89**, 22–32.
21 K. V. K. Rao and L. Iyengar, *Acta Crystallogr., Sect. A*, 1969, **25**, 302–303.
22 A. V. Korotcov, Y. S. Huang, K. K. Tiong and D. S. Tsai, *J. Raman Spectrosc.*, 2007, **38**, 737–749.
23 A. L. Paulsen, F. Borup, R. W. Berg and S. Boghosian, *J. Phys. Chem. A*, 2010, **114**, 7485–7493.
24 M.-R. Gao, M. K. Y. Chan and Y. Sun, *Nat. Commun.*, 2015, **6**, 7493.
25 J. Chen, G. Liu, Y.-Z. Zhu, M. Su, P. Yin, X.-J. Wu, Q. Lu, C. Tan, M. Zhao, Z. Liu, W. Yang, H. Li, G.-H. Nam, L. Zhang, Z. Chen, X. Huang, P. M. Radjenovic, W. Huang, Z.-Q. Tian, J.-F. Li and H. Zhang, *J. Am. Chem. Soc.*, 2020, **142**, 7161–7167.
26 J. He, X. Zhou, P. Xu and J. Sun, *Adv. Energy Mater.*, 2021, **11**, 2102883.
27 S. Geiger, O. Kasian, M. Ledendecker, E. Pizzutilo, A. M. Mingers, W. T. Fu, O. Diaz-Morales, Z. Li, T. Oellers, L. Fruchter, A. Ludwig, K. J. J. Mayrhofer, M. T. M. Koper and S. Cherevko, *Nat. Catal.*, 2018, **1**, 508–515.
28 P. Singh and M. S. Hegde, *Chem. Mater.*, 2009, **21**, 3337–3345.
29 J. Fu, K. Yang, C. Ma, N. Zhang, H. Gai, J. Zheng and B. H. Chen, *Appl. Catal., B*, 2016, **184**, 216–222.
30 K. Islam, R. Sultana, B. Satpati and S. Chakraborty, *Vacuum*, 2022, **195**, 110675.
31 Y. Zhang, Y. Zhang, Z. Zeng and D. Ho, *Mater. Horiz.*, 2023, **10**, 2904–2912.

32 H. Liu, Z. Zhang, J. Fang, M. Li, M. G. Sendeku, X. Wang, H. Wu, Y. Li, J. Ge, Z. Zhuang, D. Zhou, Y. Kuang and X. Sun, *Joule*, 2023, **7**, 558–573.
33 N. Zhang and Y. Chai, *Energy Environ. Sci.*, 2021, **14**, 4647–4671.
34 D. Antipin and M. Risch, *Electrochem. Sci. Adv.*, 2023, **3**, e2100213.
35 W. Li, F. Li, H. Yang, X. Wu, P. Zhang, Y. Shan and L. Sun, *Nat. Commun.*, 2019, **10**, 5074.
36 W. Gou, Z. Xia, X. Tan, Q. Xue, F. Ye, S. Dai, M. Zhang, R. Si, Y. Zou, Y. Ma, J. C. Ho and Y. Qu, *Nano Energy*, 2022, **104**, 107960.
37 R. Šimpraga, G. Tremiliosi-Filho, S. Y. Qian and B. E. Conway, *J. Electroanal. Chem.*, 1997, **424**, 141–151.
38 B. Zhou, Y. Li, Y. Zou, W. Chen, W. Zhou, M. Song, Y. Wu, Y. Lu, J. Liu, Y. Wang and S. Wang, *Angew. Chem., Int. Ed.*, 2021, **60**, 22908–22914.
39 N. Cong, Y. Han, L. Tan, C. Zhai, H. Chen, J. Han, H. Fang, X. Zhou, Y. Zhu and Z. Ren, *J. Electroanal. Chem.*, 2021, **881**, 114955.
40 K. Klyukin, A. Zagalskaya and V. Alexandrov, *J. Phys. Chem. C*, 2019, **123**, 22151–22157.
41 K. K. Rahangdale and S. Ganguly, *Phys. B*, 2022, **626** 413570.
42 X. Wang, H. Zhong, S. Xi, W. S. V. Lee and J. Xue, *Adv. Mater.*, 2022, **34**, 2107956.
43 Y. Wang, J. Wu, G. Wang, D. Yang, T. Ishihara and L. Guo, *Appl. Catal., B*, 2021, **285**, 119873.
44 Y. S. Huang and F. H. Pollak, *Solid State Commun.*, 1982, **43**, 921–924.
45 A. Rahman, S. Mondal, M. Modak, A. Singh, N. S. Thayat, H. Singh, J. K. Clegg, H. K. Poswal, V. Haridas and S. P. Thomas, *Small*, 2024, 2402120.